Large-Eddy Simulation of airborne wind energy systems wakes

Large-Eddy Simulation of airborne wind energy systems wakes

J-B Crismer, F Trigaux, M Duponcheel and G Winckelmans

Institute of Mechanics, Materials and Civil Engineering (iMMC), Université catholique de Louvain (UCLouvain), 1348 Louvain-la-Neuve, Belgium

E-mail: jean-baptiste.crismer@uclouvain.be

Abstract. Wind energy is usually harnessed using wind turbines but it is not the only way of collecting this energy. In this paper, Airborne Wind Energy Systems (AWES) are considered. The understanding of the wake shed by such devices is of primary importance when considering farms, yet it has not been much studied so far, and even less so when considering kites with soft curved wing. In this work, LES is used to analyse the wake of AWES. Two types of wings are considered: a straight wing, modelling the reference rigid wing AWES and a curved wing accounting for leading edge inflatable kites. Both types of wings are modelled using actuator lines. The wake analysis reveals that the wake of curved wings tends to be stronger and to recover faster. For the case of the tilted trajectory, asymmetries in the wake are also noted. The difference is explained by the azimuthal variation of the circulation distribution on the wing. It also relates to some wakes characteristics for tilted wind turbines. The wake of the curved wing is also more sensitive to the variation of the loading when it flies tilted trajectory, due to the varying loading on its tips.

1. Introduction

The recent climate objectives put forward the need for alternative energy sources. Wind energy gained much interest during the last decades and now constitutes a cornerstone to meet the climate objectives [1]. The installed wind power capacity has increased significantly and is projected to keep growing even faster. Nowadays, this energy is mostly harnessed using wind turbines. However other devices can be used to extract energy from the wind. Airborne Wind Energy Systems (AWES) are based on tethered wings. Their main advantage is that they require less infrastructure compared to conventional wind turbines and can harvest power from higher altitude winds. The technology is still emerging and has not yet been studied in great details even if it is gaining more and more interest. Different types of wings can be used, ranging from rigid to soft kite wings [2]. AWES also have several operation modes and they can be divided into two main categories: *lift mode* (or *ground-gen*) and *drag mode* (or *fly-gen*). In lift mode, the electricity generation takes place at the ground. The kite moves away from its anchor point, pulling on a cable that unwinds from a drum connected to a generator during the reel-out phase. The kite then comes back during the reel-in phase, and the cable winds back on the drum. Drag mode AWES generate electricity directly on the wing, using wing-mounted turbines. The electricity is then sent to the ground through the tether.

This work focuses on lift mode AWES and aims at studying their impact on the airflow they encounter. Two types of wing are studied: straight and curved wings. The straight wing

is representative of rigid wing AWES while the curved wing is used to model soft wing kites. The study of the wake of such wind energy extracting devices is of importance as it greatly modifies the atmospheric flow velocity field and structures, which can have a significant impact on other devices downstream; hence also for the energy yield of a wind farm. The wake of conventional wind turbines has already been extensively studied and their dynamics is a well-known phenomenon [3]. However, studies of AWES wakes are scarce. In a study of Haas [4], lift and drag mode AWES wakes were studied and compared. However, this study only considered straight wings. Soft wing kites have an anhedral curvature and the wake produced by such curved-shaped AWES has not been studied yet. This paper aims at gaining insights regarding lift mode AWES wakes and at contributing to filling the gap concerning curved wings.

In this study, we consider the wake of single wings, straight or curved, and following simplified trajectories: non-tilted and tilted circular paths, relatively to the wind direction, at constant rotation speed and tether length. The methodology is presented in Section 2 and the results are presented and discussed in Section 3. The last section presents the conclusion and provides some perspectives for future research.

2. Methodology

2.1. Flow solver

Large-eddy simulation (LES) is performed using an in-house fourth-order finite difference solver [5, 6] running on high performance computing infrastructures. The code solves the incompressible Navier-Stokes equations. It has been validated against direct numerical simulations (DNS) in [5]. The subgrid-scale model used here for LES is a regularized variational multiscale (RVM) [7, 8]. The mesh is a cartesian staggered grid and the time integration is performed using a second order Adams-Bashforth scheme. The turbulence in the inflow is taken into account using Mann boxes [9], where the velocity fluctuations are pre-calculated using the Mann algorithm and injected at the inlet.

2.2. Wing models

The wings are modelled using actuator curves, an extension of the actuator line method to curved blades. This "actuator curve method" (ACM) has already been used for aeroelastic simulations of horizontal axis wind turbines (HAWT) [10]. The original method [11] is generalized to handle parametric curves [12]. This method has three main steps. Firstly, the effective flow velocity is interpolated from the grid to the actuator curve control points. Secondly, the aerodynamic forces are computed using the obtained velocities and the airfoil polar data. Finally, the forces are distributed on the flow grid and taken into account via a volumic force term added to the flow equations.

It has been shown that the use of a 2D regularization kernel for both the velocity evaluation at the control points and the force distribution better predicts the aerodynamic forces than when using a 3D kernel [13]. Here, a 2D Gaussian kernel

$$\eta_{2\mathrm{D}} = \frac{1}{\pi\,\sigma^2}\exp\left(-\frac{d^2}{\sigma^2}\right) \tag{1}$$

is used in a 2-D planar grid perpendicular to the actuator line, where d is the 2-D distance to the control point and σ is the width of the Gaussian. A template containing the distribution points with their pre-computed Gaussian weights is used, see [10]. Linear interpolation is used to transfer velocity information from the flow grid to the template, and to transfer force information from the template to the flow grid.

2.3. Numerical setup

We first remind some definitions. The *span* b is the distance from tip to tip. The *surface* S is the surface projected on a plane parallel to the inflow velocity direction and the span vector when the wing has a zero angle of attack i.e. $\int_{-b/2}^{b/2} c(y)\,dy$, where c is the chord length and y is the coordinate along the straight line going from tip to tip. The *length* l of the wing is the distance from tip to tip when following the wing curvature. Finally, the *wetted surface* S_w is the wing surface when considered unfolded i.e. $\int_{-l/2}^{l/2} c(s)\,ds$, where s the parametric coordinate along the curved surface from tip to tip.

In this work, two wings are studied. The first one is a *straight wing* (SW), representing the rigid wing reference AWES described in [14]. This AWES has a wing span of 42.5 m and an aspect ratio of $AR = b^2/S = 12$. For this study, it has been scaled up to a wingspan of 48 m. The second wing is curved, and it is inspired from the leading edge inflatable kite LEIV3 [15, 16]. The original wing has a span of 8.3 m and an aspect ratio of 3.35. Here, it has also been scaled to a span of 48 m. It will be called the *curved wing* (CW). The different wing geometries are represented in Figure 1 and some key dimensions are reported in Table 1. The wakes of those wings are studied in the case of non-tilted and tilted trajectories.

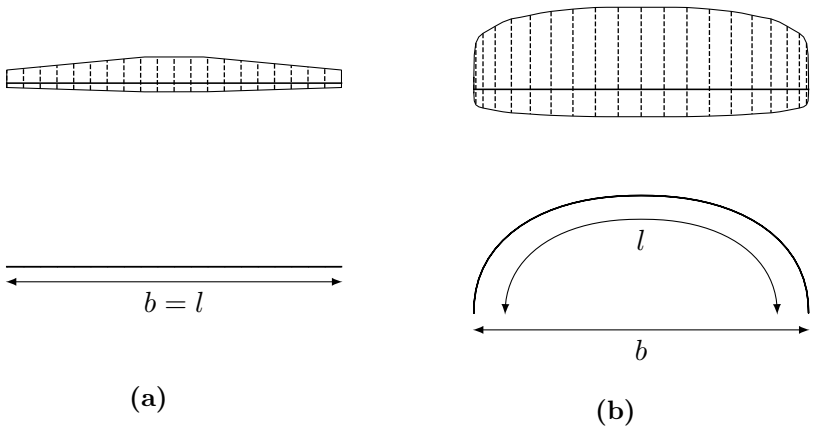

Figure 1: Wings geometries: straight wing (a) and curved wing (b) of same span b.

Table 1: Wings dimensions.

Wing type	Span b [m]	Projected surface S [m^2]	AR	Length l [m]	Wetted surface S_w [m^2]
Straight wing	48	190.7	12	48	190.7
Curved wing	48	687.1	3.35	65.84	860.9

In each case studied, the wings fly a circular trajectory at tilt angle γ of 0° or 19°. The radius R of the trajectory is $R = 2.5\,b$. The flow is driven by imposing a mean flow velocity U_∞=10 m/s at the inflow, and with added turbulence. The wings rotate clockwise at a speed such that they have an outer tip speed ratio $\lambda = \frac{\Omega\,(R+b/2)}{U_\infty} \simeq 7$; the centre of the wing then has a rotation velocity of 58.9 m/s. The angle of attack of the wing with $(\Omega r + U_\infty)$ are chosen

such that it is 3° below the polar (showed in the provided references) stall angle on the middle of the wings. The size of the domain is $9\,D \times 3\,D \times 3\,D$, where $D = 2R$ is the diameter of the trajectory, with $768 \times 256 \times 256$ grid points. It thus correspond to approximately 85 points per D or 17 points per b. The resolution is similar to that used in the AWES wake simulations by Haas [17], where a grid refinement study had shown the ability of such resolution to capture the main wake features. It is also similar to that used in a study by Trigaux [18] where wakes from tilted HAWT were investigated using the same flow solver and ACM as used here. The domain is sketched in Figure 2. We use periodic and no slip boundary conditions in the transverse and vertical directions, respectively. An outflow boundary condition is used at the end of the domain, in the streamwise direction. The turbulence is injected in the domain through a $12\,D$ long Mann box with a turbulence intensity of 6%, using the Kaimal spectrum. The wake flow is measured, downstream of the centre of rotation, in vertical planes from $1\,D$ to $5\,D$. The flow statistics are accumulated over two Mann box flow through times (thus $24\,t^*$ where $t^* = \frac{U\,t}{D}$) and after it has developed for $12\,t^*$. The kite velocity is such that it does 22.5 revolutions over a Mann box flow through time; this was done on purpose to avoid that it encounters twice exactly the same turbulent flow features.

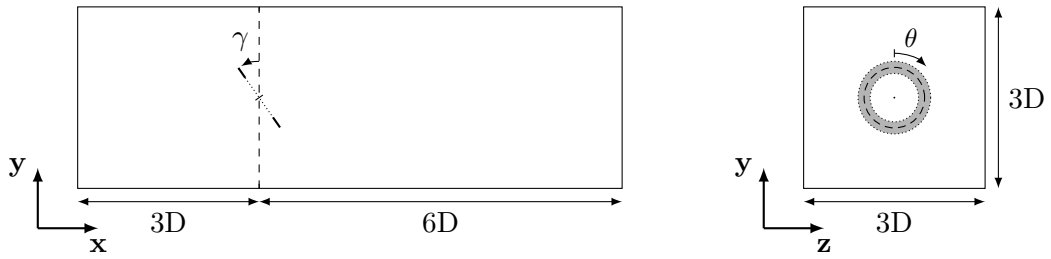

Figure 2: Computational domain with its relative dimensions, where x is the streamwise , y is the vertical and z the transverse direction.

3. Results

3.1. Non-tilted trajectory

This section presents the results for a non-tilted trajectory. Since the curved wing has a larger surface area than the straight wing, it has more lift, and the velocity deficit is therefore greater. The wake velocity and vorticity data obtained for the curved wing are hence scaled by the ratio of the average force in the flow direction, $F_{\mathrm{x},SW}/F_{\mathrm{x},CW} = 0.45$, and then compared to wake velocity and vorticity data obtained for the straight wing.

The analysis of the wake starts with the time-averaged velocity profiles, as shown in Figure 3 where $\Delta U = U - U_{x=-1\,D}$. The scaled deficit intensity is slightly higher at $1\,D$ downstream for the curved wing. It then decreases a bit faster than for the straight wing when moving downstream. This also causes the low velocity annulus to spread more quickly into a fully filled circular wake.

The axial velocity deficit in cross-flow planes are presented in Figure 4. As in the previous figure, the stronger velocity deficit can be observed for the curved wing, together with its faster mixing. As there is no tilting, the wake is nearly axisymetric in both cases.

Volume renderings of the vorticity fields are shown in Figure 5, the vorticity intensity being scaled for the curved wing so as to provide a better comparison with the straight wing. The way the tip vortices distort and eventually desegregate is found to be quite similar in both cases.

For the sake of comparison, the cases with titled trajectory are already shown in the same figure. The observation are the same than for the non-tilted trajectory; the main difference being that the wakes are also deflected downward.

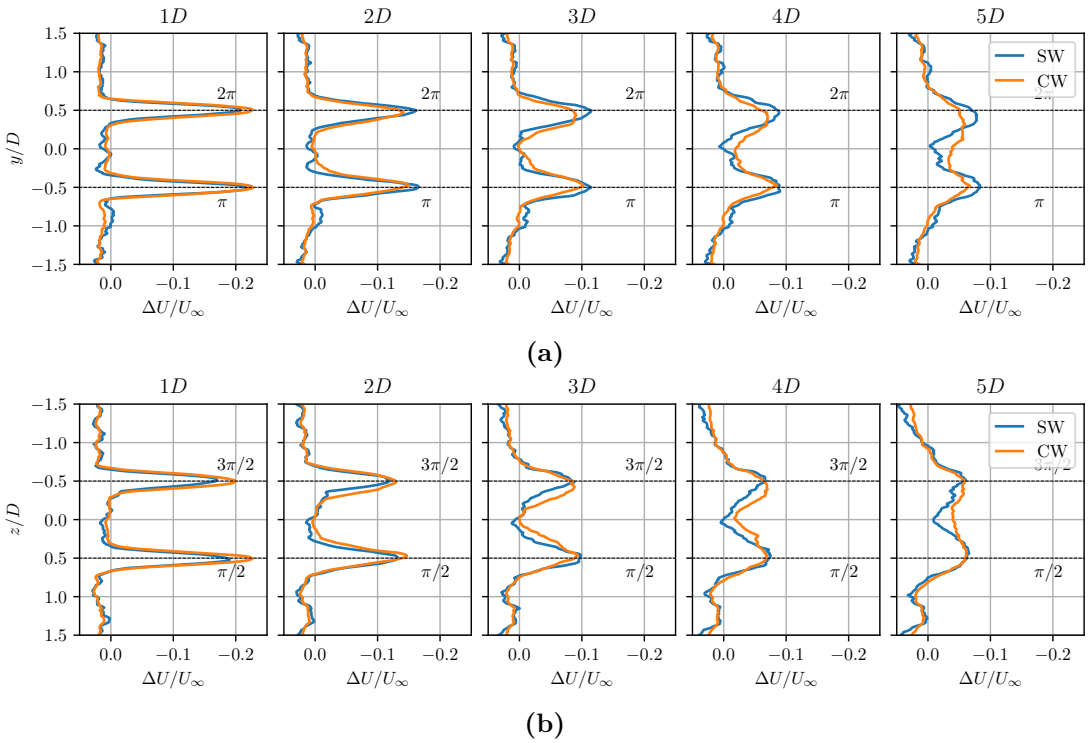

Figure 3: Time-averaged velocity profiles in the vertical (a) and horizontal (b) directions, at several downstream positions: straight wing (—) and curved wing (—) flying a trajectory without tilt angle. For the curved wing, the velocity deficit was scaled using $F_{\mathrm{x},SW}/F_{\mathrm{x},CW} = 0.45$.

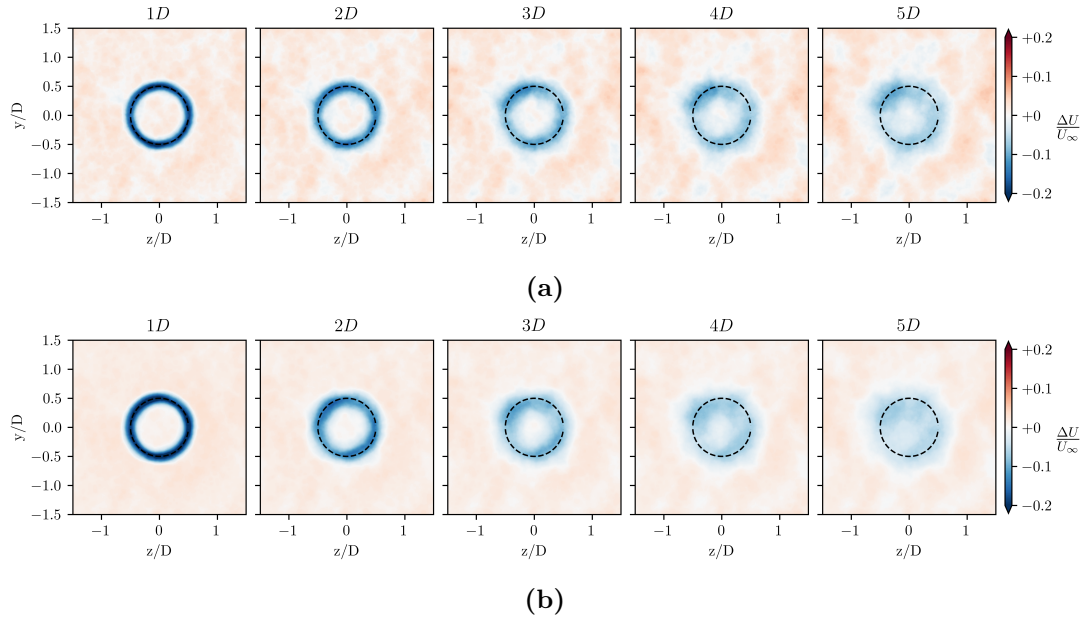

Figure 4: Time-averaged velocity deficit at several downstream positions: straight wing (a) and curved wing (b) flying a trajectory without tilt angle. For the curved wing, the velocity deficit was scaled using $F_{\mathrm{x},SW}/F_{\mathrm{x},CW} = 0.45$.

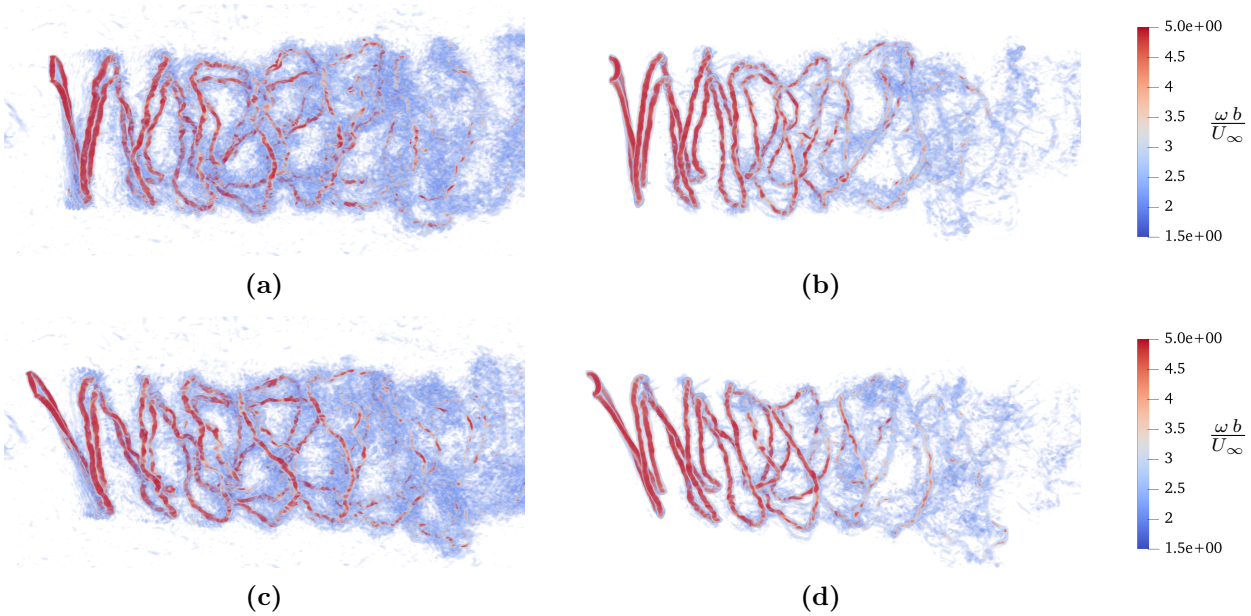

Figure 5: Volume rendering of the dimensionless vorticity magnitude at $t^* = 24$: straight wing (a) and curved wing (b) flying a trajectory without tilt angle; and also flying a trajectory at 19° tilt angle (c-d). For the curved wing, the vorticity was scaled using $F_{\mathrm{x},SW}/F_{\mathrm{x},CW} = 0.45$.

3.2. Tilted trajectory

When the wing's rotational plane is tilted, as is the case for real AWES connected to the ground by a tether, the wake is no longer axisymmetric. The vertical and horizontal velocity deficit profiles are provided in Figure 6. As seen from the vertical profile, the tilted rotation plane causes the velocity deficit to be more important on the lower part of the loop. This effect was also reported by Haas in [17]. Similarly to tilted wind turbines, the wakes are redirected downward [18]. In addition, the upper part of the wake is more deflected than the lower part. The deflection also occurs a bit faster in the case of the curved wing. At $1\,D$ downstream, the deficit on the lower part of the loop is slightly larger in the case of the curved wing, and is also wider; however the deficit is a bit weaker on the upper side of the loop.

The horizontal velocity deficit profile in Figure 6b is almost symmetrical at $1\,D$. A slight difference appears between the left ($\pi/2$) and right ($3\pi/2$) parts while moving downstream. The right part of the deficit becomes larger. This is more also pronounced for the curved wing.

The axial velocity deficit in cross-flow planes are plotted in Figure 7. As observed in the velocity profiles, the difference between the two wings is the presence of a lower velocity deficit at the top of the loop for the curved wing. Also, Figure 7b shows that the larger velocity deficit occurring at the lower part of the loop ($1\,D$ downstream) tends to rotate counter-clockwise while being advected downstream. This may explain the evolution of the velocity deficit profile in the horizontal direction (this larger deficit moving towards the $\pi/2$ position) as the wake is rotating in the direction opposite to that of the kite, as it does for wind turbines.

The faster redirection of the upper part of the loop for the curved wing is clearly identifiable in Figure 8, where the velocity deficit is plotted in the $x-y$ plane. As mentioned previously, the deficit is also larger and wider for the lower part of the loop, and it expands faster when moving downstream. This happens for both wings, but this is stronger for the curved wing.

The force normal to the rotation plane and the force parallel to the inflow are provided in Figure 9. The forces are made dimensionless using $\left(\rho U_\infty^2/2\right) S$. The normal force varies like a

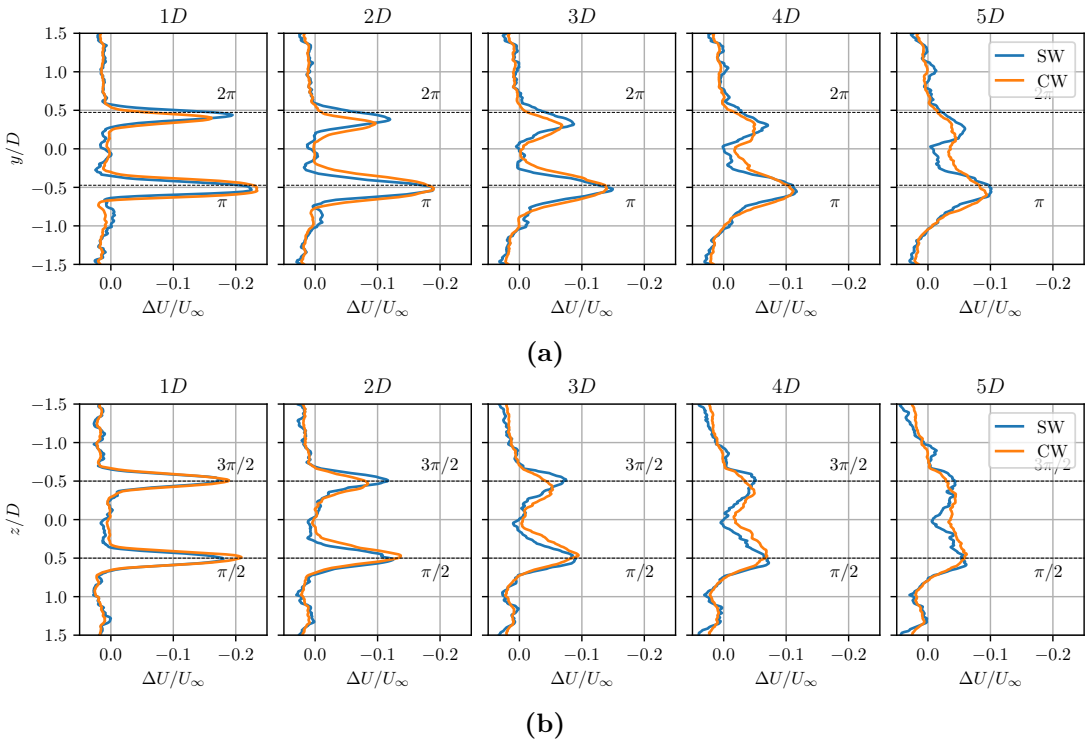

Figure 6: Time-averaged velocity profiles in the vertical (a) and horizontal (b) directions, at several downstream positions: straight wing (—) and curved wing (—) flying a trajectory with 19° tilt angle. For the curved wing, the velocity deficit was scaled using $F_{\mathrm{x},SW}/F_{\mathrm{x},CW} = 0.45$.

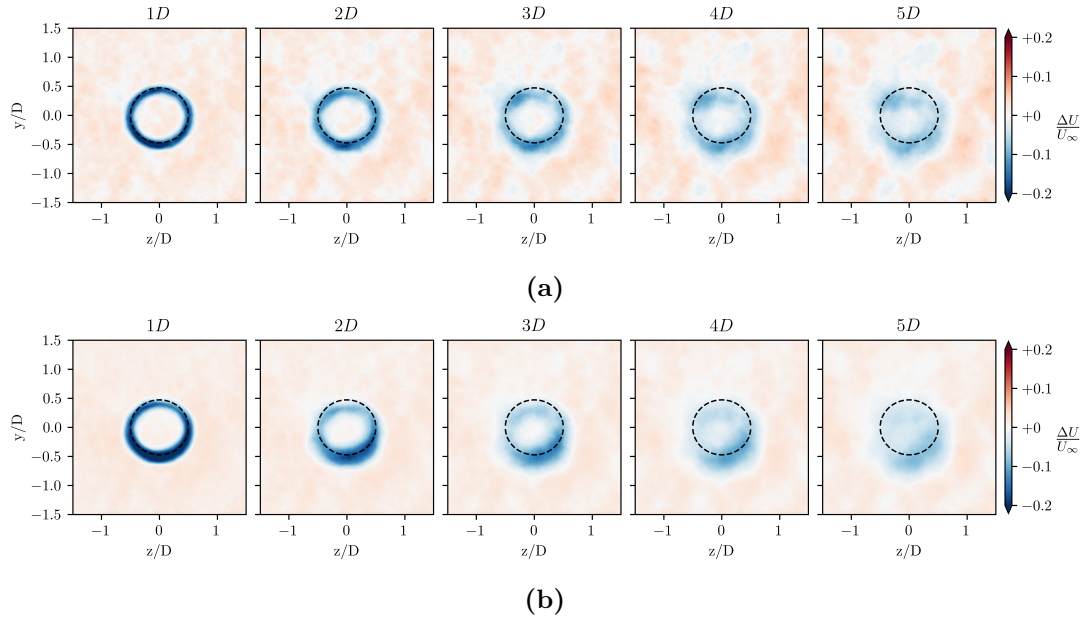

Figure 7: Time-averaged velocity deficit at several downstream positions: straight wing (a) and curved wing (b) flying a trajectory with 19° tilt angle. For the curved wing, the velocity deficit was scaled using $F_{\mathrm{x},SW}/F_{\mathrm{x},CW} = 0.45$.

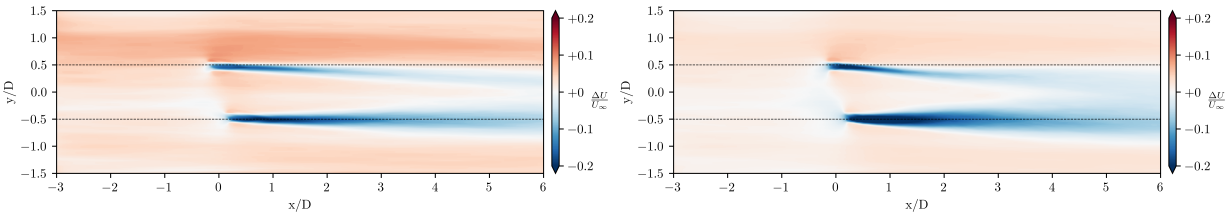

(a) **(b)**

Figure 8: Time-averaged velocity deficit in the vertical plane: straight wing (a) and curved wing (b) flying a trajectory with 19° tilt angle. For the curved wing, the velocity was scaled using $F_{\mathrm{x},SW}/F_{\mathrm{x},CW} = 0.45$.

sine because Ωr decreases and increases the relative wind seen by the wing at $\pi/2$ and $3\pi/2$, respectively. For the force in the inflow direction, this effect is supplemented with the variation of the force acting on the tips in the case of the curved wing. For the non-tilted trajectory, the tips have no angle of attack because they are aligned with U_∞. When the trajectory is tilted, the force acting on the tips varies with θ: it is still null at $\pi/2$ and $3\pi/2$ but it is maximal or minimal (depending on which tip is considered) at 0 and π. As depicted in Figure 10, at the 0 azimuthal position the angle of attack decreases at the outer tip and it increases at the inner tip. But, the relative velocity is larger on the outer tip than on the inner tip. The forces on the tips thus balance each other and there is only a small radial force at this position. At π, the inner tip has a lower angle of attack and a smaller relative velocity than the outer tip; there is thus a net radial force which contributes to the axial force when at that position.

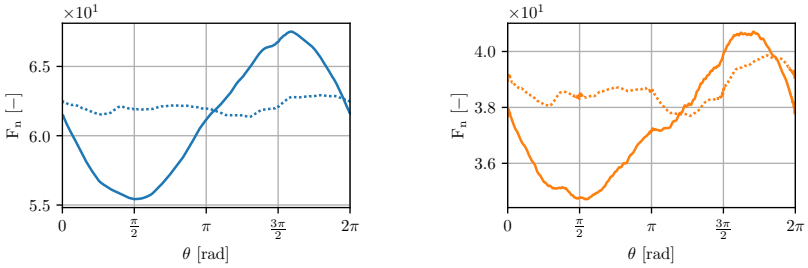

(a)

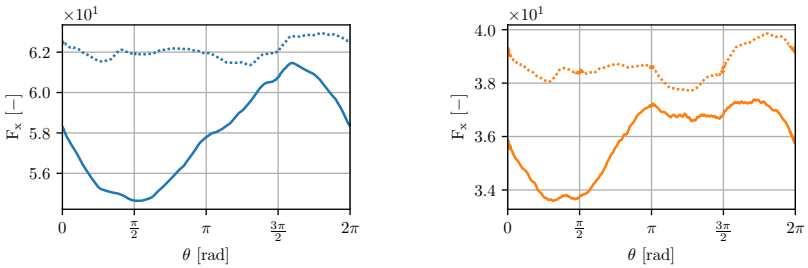

(b)

Figure 9: Phase-averaged azimuthal evolution of (a) the force normal to the rotation plane and (b) the force parallel to the inflow: straight wing (—) and curved wing (—) flying on a tilted trajectory (solid) and on a non-tilted trajectory (dot).

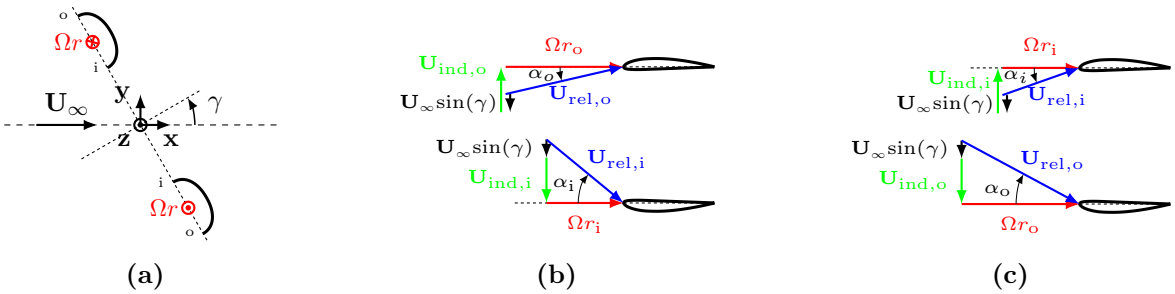

Figure 10: Schematic explaining the difference in angle of attack at the curved wing tips, depending on its azimuthal position. Curved wing at the upper and lower azimuthal positions (a), velocity triangle when at the upper position (b) and when at the lower position (c).

Those forces may not fully explain the difference in velocity deficit between the 0 and π since there is no large force difference between those positions. Another possible explanation is the variation of the circulation distribution $\Gamma(s)$ on the wing (where s is the parametric coordinate along the wing length), that also influences the wake. The difference between the upper and lower positions, observed for both wings, might be due to the variation of the circulation distribution with the azimuthal position. The circulation is proportional to the lift force acting on the wing and thus $d\Gamma/d\theta \propto dL/d\theta \simeq dF_n/d\theta$. Examining the normal force distribution, we obtain $dF_n/d\theta < 0$ at the 0 position and $dF_n/d\theta > 0$ at π, which might play a role in the difference in the velocity deficit. This is similar to tilted horizontal axis wind turbines where a velocity deficit difference between the upper and lower part of the rotor is also observed [18].

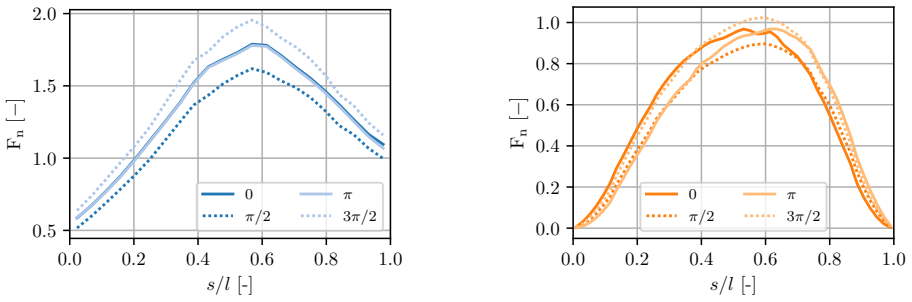

Figure 11: Phase-averaged normal force distribution on (a) the straight wing (—) and (b) the curved wing (—) at several azimuthal positions. Dark solid (—), dark dotted (···), light solid (—) and light dotted (···) respectively stand for the 0, $\pi/2$, π, $3\pi/2$ positions. s is the parametric coordinate along the wing length.

The wake is also influenced by the tip vortices. Their intensity is proportional to the variation of circulation along the wing span, and thus of the normal force distribution. The variation of the angle of attack at the tips as a function of the azimuthal angle influences the loading distribution on the wing. The mean location for the centre of the loading distribution is not located at the middle of the wing because the wing feels an increasing relative velocity as the distance from the center of rotation increases; the distribution is thus skewed. When the tip loading increases, the loading is further shifted to that tip, increasing $d\Gamma/ds$, hence increasing the shed tip vortex strength. As explained above, the outer tip loading increases significantly at $\theta = \pi$. As shown in Figure 11, this shifts the load distribution to the outer tip and it therefore increases the shed

tip vortex intensity. This could also explain the larger expansion of the wake deficit at the lower part of the loop in the case of the curved wing.

4. Conclusion

In this paper, LES was used to simulate AWESs and analyse their wake. Two types of wings were studied: a straight wing, modelling the reference rigid wing AWES described in [14] and a curved wing inspired from the LEIV3 kite from TUDelft [15, 16]; both being modelled using actuator lines. The results indicate that, even when normalised to take into account the difference in force for proper comparison, the velocity deficit of the curved wing tends to be a bit stronger in the near wake, with stronger tip vortices; yet it also decreases a bit faster. For the case with tilted trajectory, asymmetries are observed in the wake. Both wing wakes are stronger on the lower part of the loop, which seems to be related to the azimuthal variation of the circulation distribution over the wing span. The curved wing wake expansion is particularly large on the lower part of the loop; a possible explanation relates to the loading distribution due to the variation of the loading on the curved tips.

In this study, we simulated AWES wings flying on a closed circular path: first non-tilted and then tilted relatively to the upstream flow. A next step will be to simulate such wings flying full power cycles, with realistic reel-out and reel-in phases, and to also investigate their wakes. AWES wings flying with optimised flight parameters should then also be investigated.

It will furthermore be interesting to compare the fully developed far wake of AWES to that of HAWT: hence after the turbulence in the expanding annular wake has reached the center of the disk of diameter D and has further attained a statistical equilibrium; which will occur further than the last plane investigated here ($x = 5\,D$). This is also left to future work.

5. Acknowledgements

This work is carried out as part of the BORNE project on "Developing the tools and insight to expand the Belgian offshore wind farms with airborne wind energy systems", funded by the Energy Transition Funds from the SPF Economy. The present research benefited from computational resources made available on the Tier-1 supercomputer of the Fédération Wallonie-Bruxelles, infrastructure funded by the Walloon Region under the grant agreement n°1117545. Computational resources were also provided by the supercomputing facilities of the Université catholique de Louvain (CISM/UCLouvain) and the Consortium des Équipements de Calcul Intensif en Fédération Wallonie Bruxelles (CÉCI) funded by the Fond de la Recherche Scientifique de Belgique (F.R.S.-FNRS) under convention 2.5020.11 and by the Walloon Region.

6. References

[1] European Commission 2019 *The European Green Deal* COM(2019) 640 (Brussels)
[2] Cherubini A, Papini A, Vertechy R and Fontana M 2015 Airborne wind energy systems: A review of the technologies *Renewable and Sustainable Energy Reviews* **51** 1461–1476 ISSN 1364-0321
[3] Porté-Agel F, Bastankhah M and Shamsoddin S 2020 Wind-turbine and wind-farm flows: A review *Boundary-Layer Meteorology* **174** 1–59
[4] Haas T and Meyers J 2017 Comparison study between wind turbine and power kite wakes *Journal of Physics: Conference Series* **854** 012019
[5] Duponcheel M, Bricteux L, Manconi M, Winckelmans G and Bartosiewicz Y 2014 Assessment of rans and improved near-wall modeling for forced convection at low prandtl numbers based on les up to Re_τ=2000 *International Journal of Heat and Mass Transfer* **75** 470–482
[6] Moens M, Duponcheel M, Winckelmans G and Chatelain P 2018 An actuator disk method with tip-loss correction based on local effective upstream velocities *Wind Energy* **21** 766–782
[7] Jeanmart H and Winckelmans G 2007 Investigation of eddy-viscosity models modified using discrete filters: A simplified "regularized variational multiscale model" and an "enhanced field model" *Physics of Fluids* **19** 055110

[8] Cocle R, Bricteux L and Winckelmans G 2009 Scale dependence and asymptotic very high reynolds number spectral behavior of multiscale subgrid models *Physics of Fluids* **21** 085101
[9] Mann J 1994 The spatial structure of neutral atmospheric surface-layer turbulence *Journal of Fluid Mechanics* **273** 141–168
[10] Trigaux F, Chatelain P and Winckelmans G 2022 A flexible actuator curve model for aeroelastic simulations of wind turbines in atmospheric boundary layers *Journal of Physics: Conference Series* **2265** 022050
[11] Sørensen J N and Shen W Z 2002 Numerical modeling of wind turbine wakes *Journal of Fluids Engineering* **124** 393–399 ISSN 0098-2202
[12] Jha P K and Schmitz S 2018 Actuator curve embedding – an advanced actuator line model *Journal of Fluid Mechanics* **834** R2
[13] Caprace D G, Winckelmans G and Chatelain P 2020 An immersed lifting and dragging line model for the vortex particle-mesh method *Theoretical and Computational Fluid Dynamics* **34** 21–48
[14] Eijkelhof D, Rapp S, Fasel U, Gaunaa M and Schmehl R 2020 Reference design and simulation framework of a multi-megawatt airborne wind energy system *Journal of Physics Conference Series* **1618** 32020
[15] Oehler J and Schmehl R 2018 Aerodynamic characterization of a soft kite by in situ flow measurement *Wind Energy Science* **4** 1–21
[16] Folkersma M, Schmehl R and Viré A 2019 Boundary layer transition modeling on leading edge inflatable kite airfoils *Wind Energy* 1–14
[17] Haas T, De Schutter J, Diehl M and Meyers J 2019 Wake characteristics of pumping mode airborne wind energy systems *Journal of Physics: Conference Series* **1256** 012016
[18] Trigaux F, Moens M, Chatelain P and Winckelmans G 2020 Tilted wind turbines in farm configuration for improved global efficiency *Journal of Physics: Conference Series* **1618** 062035